Accurate effective atomic number determination with polychromatic grating-based phase-contrast computed tomography

Lorenz Birnbacher,[1,*] Marian Willner,[1,2,3] Mathias Marschner,[1] Daniela Pfeiffer,[2] Franz Pfeiffer,[1,2,4] and Julia Herzen[1]

[1] *Chair of Biomedical Physics, Department of Physics and Munich School of BioEngineering, Technical University of Munich, 85748 Garching, Germany*
[2] *Department of Diagnostic and Interventional Radiology, Klinikum rechts der Isar, Technical University of Munich, 81675 München, Germany*
[3] *MITOS GmbH, 85748 Garching, Germany*
[4] *Institute for Advanced Study, Technical University of Munich, 85748 Garching, Germany*
[*] *lorenz.birnbacher@ph.tum.de*

Abstract: The demand for quantitative medical imaging is increasing in the ongoing digitalization. Conventional computed tomography (CT) is energy-dependent and therefore of limited comparability. In contrast, dual-energy CT (DECT) allows for the determination of absolute image contrast quantities, namely the electron density and the effective atomic number, and is already established in clinical radiology and radiation therapy. Grating-based phase-contrast computed tomography (GBPC-CT) is an experimental X-ray technique that also allows for the measurement of the electron density and the "effective atomic number. However, the determination of both quantities is challenging when dealing with polychromatic GBPC-CT setups. In this paper, we present how to calculate the effective atomic numbers with a polychromatic, laboratory GBPC-CT setup operating between 35 and 50 kVp. First, we investigated the accuracy of the measurement of the attenuation coefficients and electron densities. For this, we performed a calibration using the concept of effective energy. With the reliable experimental quantitative values, we were able to evaluate the effective atomic numbers of the investigated materials using a method previously shown with monochromatic X-ray radiation. In detail, we first calculated the ratio of the electron density and attenuation coefficient, which were experimentally determined with our polychromatic GBPC-CT setup. Second, we compared this ratio with tabulated total attenuation cross sections from literature values to determine the effective atomic numbers. Thus, we were able to calculate two physical absolute quantities – the electron density and effective atomic number – that are in general independent of the specific experimental conditions like the X-ray beam spectrum or the setup design.

OCIS codes: (170.3880) Medical and biological imaging; (340.7450) X-ray interferometry; (110.7440) X-ray imaging; (180.7460) X-ray microscopy; (170.6960) Tomography.

References and links

1. F. Sardanelli, "Trends in radiology and experimental research," Eur. Radiol. Exp. **1**, 1 (2017).
2. J. P. Schlomka, E. Roessl, R. Dorscheid, S. Dill, G. Martens, T. Istel, C. Bäumer, C. Herrmann, R. Steadman, G. Zeitler, A. Livne, and R. Proksa,"Experimental feasibility of multi-energy photon-counting K-edge imaging in pre-clinical computed tomography," Phys. Med. Biol. **53**(15), 4031–4047 (2008).
3. D. T. Boll, N. A. Patil, E. K. Paulson, E. M. Merkle, W. N. Simmons, S. A. Pierre, and G. M. Preminger, "Renal stone assessment with dual-energy multidetector CT and advanced postprocessing techniques: Improved characterization of renal stone composition—pilot study," Radiology **250**(3), 813–820 (2009).
4. G. Hidas, R. Eliahou, M. Duvdevani, P. Coulon, L. Lemaitre, O. N. Gofrit, D. Pode, and J. Sosna, "Determination of renal stone composition with dual-energy CT: In vivo analysis and comparison with X-ray diffraction," Radiology **257**(2), 394–401 (2010).

5. S. Leng, A. Huang, J. M. Cardona, X. Duan, J. C. Williams, and C. H. McCollough, "Dual-energy CT for quantification of urinary stone composition in mixed stones: A phantom study," Am. J. Roentgenol. **207**(2), 321–329 (2016).

6. A. Spek, F. Strittmatter, A. Graser, P. Kufer, C. Stief, and M. Staehler, "Dual energy can accurately differentiate uric acid-containing urinary calculi from calcium stones," World J. Urol. **34**(9), 1297–1302 (2016).

7. T. Bongartz, K. N. Glazebrook, S. J. Kavros, N. S. Murthy, S. P. Merry, W. B. Franz, C. J. Michet, B. M. Akkara Veetil, J. M. Davis, T. G. Mason, K. J. Warrington, S. R. Ytterberg, E. L. Matteson, C. S. Crowson, S. Leng, and C. H. McCollough, "Dual-energy CT for the diagnosis of gout: an accuracy and diagnostic yield study," Ann. Rheum. Dis. **74**(6), 1072–1077 (2014).

8. J. Henes, M. Fuld, E. Fishman, M. Horger, and J. Fritz, "Dual-energy computed tomography of the knee, ankle, and foot: Noninvasive diagnosis of gout and quantification of monosodium urate in tendons and ligaments, Semin. Musculoskelet. Radiol. **20**(01), 130–136 (2016).

9. B. Y. Hur, J. M. Lee, W. Hyunsik, K. B. Lee, I. Joo, J. K. Han, and B. I. Choi, "Quantification of the fat fraction in the liver using dual-energy computed tomography and multimaterial decomposition," J. Comput. Assist. Tomogr. **38**(6), 845–852 (2014).

10. T. Hyodo, M. Hori, P. Lamb, K. Sasaki, T. Wakayama, Y. Chiba, T. Mochizuki, and T. Murakami, "Multimaterial decomposition algorithm for the quantification of liver fat content by using fast-kilovolt-peak switching dual-energy CT: Experimental validation," Radiology **282**(2), 381–389 (2017).

11. J. K. van Abbema, M.-J. van Goethem, M. J. W. Greuter, A. van der Schaaf, S. Brandenburg, and E. R. van der Graaf, "Relative electron density determination using a physics based parameterization of photon interactions in medical DECT," Phys. Med. Biol. **60**(9), 3825–3846 (2015).

12. R. E. Alvarez and A. Macovski, "Energy-selective reconstructions in X-ray computerised tomography," Phys. Med. Biol. **21**(5), 733–744 (1976).

13. M. Torikoshi, T. Tsunoo, M. Sasaki, M. Endo, Y. Noda, Y. Ohno, T. Kohno, K. Hyodo, K. Uesugi, and N. Yagi, "Electron density measurement with dual-energy X-ray CT using synchrotron radiation," Phys. Med. Biol. **48**(5), 673–685 (2003).

14. R. Fitzgerald, "Phase-sensitive X-ray imaging," Phys. Today **53**(7), 23–26 (2000).

15. C. David, B. Nöhammer, H. Solak, and E. Ziegler, "Differential X-ray phase contrast imaging using a shearing interferometer," Appl. Phys. Lett. **81**, 3287–3289 (2002).

16. A. Momose, "Phase-sensitive imaging and phase tomography using X-ray interferometers," Opt. Express **11**(19), 2303–2314 (2003).

17. A. Momose, "Recent advances in X-ray phase imaging," Jpn. J. Appl. Phys. **44**(9A), 6355–6367 (2005).

18. T. Weitkamp, A. Diaz, C. David, F. Pfeiffer, M. Stampanoni, P. Cloetens, and E. Ziegler, "X-ray phase imaging with a grating interferometer," Opt. Express **13**(16), 6296–6304 (2005).

19. F. Pfeiffer, M. Bech, O. Bunk, P. Kraft, E. F. Eikenberry, C. Brönnimann, C. Grünzweig, and C. David, "Hard-X-ray dark-field imaging using a grating interferometer," Nat. Mater. **7**, 134–137 (2008).

20. I. Zanette, T. Weitkamp, S. Lang, M. Langer, J. Mohr, C. David, and J. Baruchel, "Quantitative phase and absorption tomography with an X-ray grating interferometer and synchrotron radiation," Phys. Status Solidi A **208**(11), 2526–2532 (2011).

21. M. Willner, M. Bech, J. Herzen, I. Zanette, D. Hahn, J. Kenntner, J. Mohr, A. Rack, T. Weitkamp, and F. Pfeiffer, "Quantitative X-ray phase-contrast computed tomography at 82 keV," Opt. Express **21**(4), 4155–4166 (2013).

22. F. Pfeiffer, T. Weitkamp, O. Bunk, and C. David, "Phase retrieval and differential phase-contrast imaging with low-brilliance X-ray sources," Nat. Phys. **2**, 258–261 (2006).

23. J. Herzen, T. Donath, F. Pfeiffer, O. Bunk, C. Padeste, F. Beckmann, A. Schreyer, and C. David, "Quantitative phase-contrast tomography of a liquid phantom using a conventional X-ray tube source," Opt. Express **17**(12), 10010–10018 (2009).

24. Z. Qi, J. Zambelli, N. Bevins, and G.-H. Chen, "Quantitative imaging of electron density and effective atomic number using phase contrast CT," Phys. Med. Biol. **55**(9), 2669–2677 (2010).

25. T. Zhou, U. Lundström, T. Thüring, S. Rutishauser, D. H. Larsson, M. Stampanoni, C. David, H. M. Hertz, and A. Burvall, "Comparison of two X-ray phase-contrast imaging methods with a microfocus source," Opt. Express **21**(25), 30183–30195 (2013).

26. M. Willner, J. Herzen, S. Grandl, S. Auweter, D. Mayr, A. Hipp, M. Chabior, A. Sarapata, K. Achterhold, I. Zanette, T. Weitkamp, A. Sztrókay, K. Hellerhoff, M. Reiser, and F. Pfeiffer, "Quantitative breast tissue characterization using grating-based X-ray phase-contrast imaging," Phys. Med. Biol. **59**(7), 1557–1571 (2014).

27. W. Spiers, "Effective atomic number and energy absorption in tissues," Br. J. Radiol. **19**, 52–63 (1946).

28. L. Birnbacher, M. Willner, A.Velroyen, M. Marschner, A. Hipp, J. Meiser, F. Koch, T. Schröter, D.Kunka, J. Mohr, F. Pfeiffer, and J. Herzen, "Experimental realisation of high-sensitivity laboratory X-ray grating-based phase-contrast computed tomography," Sci. Rep. **6**, 24022 (2016).

29. M. Willner, G. Fior, M. Marschner, L. Birnbacher, J. Schock, C. Braun, A. Fingerle, P. B. Noël, E. J. Rummeny, F. Pfeiffer, J. Herzen, "Phase-contrast hounsfield units of fixated and non-fixated soft-tissue samples," PLoS ONE **10**(8), e0137016 (2015).

30. D. Hahn, P. Thibault, A. Fehringer, M. Bech, T. Koehler, F. Pfeiffer, and P. B. Noël, "Statistical iterative reconstruction algorithm for X-ray phase-contrast CT," Sci. Rep. **5**, 10452 (2015).

31. A. Tapfer, M. Bech, A. Velroyen, J. Meiser, J. Mohr, M. Walter, J. Schulz, B. Pauwels, P. Bruyndonckx, X. Liu, A.

Sasov, and F. Pfeiffer, "Experimental results from a preclinical X-ray phase-contrast CT scanner," Proc. Natl. Acad. Sci. **109**(39), 15691–15696 (2012).

32. F. Pfeiffer, C. Kottler, O. Bunk, and C. David, "Hard X-Ray phase tomography with low-brilliance sources," Phys. Rev. Lett. **98**, 108105 (2007).
33. A. C. Kak and M. Slaney, *Principles of Computerized Tomographic Imaging* (SIAM, 2001).
34. G. T. Herman, "Correction for beam hardening in computed tomography," Phys. Med. Biol. **24**(1), 81–106 (1979).
35. R. W. James, *The Optical Principles of the Diffraction of X-rays* (G. Bell and Sons Ltd., 1962).
36. E. C. McCullough, "Photon attenuation in computed tomography," Med. Phys. **2**(6), 307–320 (1975).
37. M. J. Berger, J. H. Hubbell, S. M. Seltzer, J. Chang, J. S. Coursey, R. Sukumar, D. S. Zucker, and K. Olsen, "XCOM: Photon cross section database," NBSIR 87–3597 (2010).
38. J. H. Hubbell, "Photon cross sections, attenuation coefficients, and energy absorption coefficients from 10 keV to 100 GeV," NSRDS, NBS29 (1969).
39. M. L. Taylor, R. L. Smith, and R. D. Franich, "Robust calculation of effective atomic numbers: The Auto-Zeff software," Med. Phys. **39**(4), 2473–4209 (2012).
40. R. C. Murty, "Effective atomic numbers of heterogeneous materials," Nature **207**, 398–399 (1965).
41. R. Nowotny,"XMuDat: Photon attenuation data on PC," IAEA-NDS-195 (1998).
42. A. Sarapata, M. Willner, M. Walter, T. Duttenhofer, K. Kaiser, P. Meyer, C. Braun, A. Fingerle, P. B. Noël, F. Pfeiffer, and J. Herzen, "Quantitative imaging using high-energy X-ray phase-contrast CT with a 70 kVp polychromatic X-ray spectrum," Opt. Express **23**(1), 523-535 (2015).
43. A. Sarapata, M. Chabior, C. Cozzini, J. I. Sperl, D. Bequé, O. Langner, J. Coman, I. Zanette, M. Ruiz-Yaniz, and F. Pfeiffer, "Quantitative electron density characterization of soft tissue substitute plastic materials using grating-based X-ray phase-contrast imaging," Rev. Sci. Instr. **85**(10), 103708 (2014).
44. H. Q. Woodard and D. R. White, "The composition of body tissues," Br. J. Radiol. **59**(708), 1209–1218 (1986).
45. Goodfellow Cambridge Ltd., http://www.goodfellow.com
46. M. Chabior, T. Donath, C. David, O. Bunk, M. Schuster, C. Schroer, and F. Pfeiffer, "Beam hardening effects in grating-based X-ray phase-contrast imaging," Med. Phys. **38**(3), 1189-–1195 (2011).

1. Introduction

Quantitative imaging in medicine is becoming more and more important as the need of reproducible data emerges with ongoing digitalization [1]. In conventional computed tomography (CT), the attenuation data or its alternative representation in Hounsfield units are energy-dependent and therefore of limited comparability. Dual energy computed tomography (DECT) related techniques including K-edge or spectral imaging are already used for improved diagnostic imaging of renal stones, gout, fat content quantification in the liver [2–10] or for body tissue characterization in radiation and particle therapy [11]. A decomposition of DECT data into two components based on Compton and photoelectric effect allows calculating the electron density and the effective atomic number, which are both physical quantities independent of the experimental conditions and are not energy dependent like the attenuation coefficient in standard computed tomography [12, 13].

Grating-based phase-contrast computed tomography (GBPC-CT) is an experimental X-ray imaging technique, which also allows to perform quantitative imaging. Three complementary image signals are retrieved in GBPC-CT: the conventional attenuation signal, the phase-contrast signal, which is highly sensitive to soft-tissue density differences, and the so-called dark-field signal, which reveals small angle-scattering in the sample [14–19]. To calculate the electron density, which is related to the phase-contrast signal, one needs to additionally determine the X-ray energy. If the experiment is performed with monochromatic synchrotron radiation, the energy is known and the resulting electron density and attenuation coefficients can be verified [20, 21].

The translation of GBPC-CT from large-scale synchrotron facilities to laboratory X-ray sources allows for new possible applications closer to industry and medicine [22]. However, the polychromatic nature of laboratory GBPC-CT makes the determination of the quantitative data more complicated. Correct electron density values can be calculated by determination of an effective energy using a calibration sample in combination with a highly sensitive laboratory GBPC-CT setup [23–26]. But still, the attenuation coefficient remains an energy-dependent quantity.

To access the effective atomic number with GBPC-CT, two different approaches have been proposed. Qi et al. [24] use an intensive calibration of a phantom for the determination of the

effective atomic number with a fit function. This method provides accurate results, but one needs complex calibration for each scan differing in parameters like the tube voltage. Additionally, the method in [24] employs an exponential fit needing highly reliable reference values, which are limited for the effective atomic number [24, 27]. Willner et al. [21] proposed to determine the ratio of the Compton scattering part of the linear attenuation coefficient with the total linear attenuation coefficient, which leads to the effective atomic number. This approach was investigated at a synchrotron source with a monochromatic energy of 82 keV.

In this paper, we apply the method proposed by Willner et al. [21] to determine the effective atomic number with an experimental laboratory GBPC-CT setup using a polychromatic X-ray source. First, we present the determined electron density values and attenuation coefficients. For that, we measured a phantom consisting of different materials in a water container at 35 kVp and 50 kVp. We calculated the effective energy of the setup by data calibration. The quantitative electron density and absorption coefficients fit well in comparison to theoretical values. Based on the previous results, we illustrate how to determine the effective atomic numbers for materials with low atomic numbers ($Z_{eff} \leq 8$). In detail, we compared the ratio of the experimentally measured electron density values over the attenuation coefficients with tabulated attenuation cross sections. The presented results of the effective atomic numbers are in good agreement with reference values. In contrast to previous methods to access the effective atomic numbers, our approach does not need that extended of calibration of the effective atomic numbers as shown in Qi et al. [24], since we only use simple effective energy calibration. In addition to Willner et al. [21], we show that the approach works with a polychromatic laboratory GBPC-CT setup increasing the range of potential applications.

Finally, we investigated the effect of beam hardening with a phantom immersed in different surrounding liquids. The differences in electron densities turned out to be small for all three experiments with different surrounding liquids. The same is valid for the differences in effective atomic numbers except for low absorbing surrounding liquids like oil, for which additional beam hardening correction was necessary.

2. Methods

2.1. Measurements and data analysis

The laboratory GBPC-CT setup (grating or Talbot-Lau interferometer) consisted of an X-ray source, three gratings, and an X-ray detector as shown in Fig. 1 and presented in full detail in [28]. The X-ray source was a rotating anode of type Enraf Nonius FR591 with a molybdenum target operating between 35 - 50 kVp and at 70 mA. For the measurement at 50 kVp, we added an aluminum filter of 1 mm thickness to harden the spectrum. Furthermore, we used a Dectris Pilatus II 100k single-photon counting detector with a 1 mm thick silicon sensor and 487×195 pixels of $172 \times 172 \, \mu m^2$ pixel size.

The phase shift of the phase grating was π at a design energy of 27 keV and the inter-grating distances were 85.7 cm. The distances were kept constant for all voltages. The gratings were binary line gratings with a period of 5.4 μm on silicon wafers. In general, the first grating, the so-called source grating, is an absorption grating providing sufficient transverse coherence for the formation of an interference pattern. The second grating, the phase-grating, creates a periodic phase modulation of the wave front. The last grating, the analyzer grating, allows one to resolve the interference pattern created by the phase-grating, which usually has a much smaller period than the detector pixel size. All gratings were fabricated by the Institut für Mikrostrukturtechnik, Karlsruhe Institute of Technology (Karlsruhe, Germany).

In order to retrieve the differential phase-contrast signal in addition to the conventional attenuation – the dark-field signal is not considered here – we used the phase stepping approach [18]. All projections were measured with 11 phase steps and an exposure time of 3 s per phase step. We applied weighted least-squares fit processing to extract the differential phase-contrast from
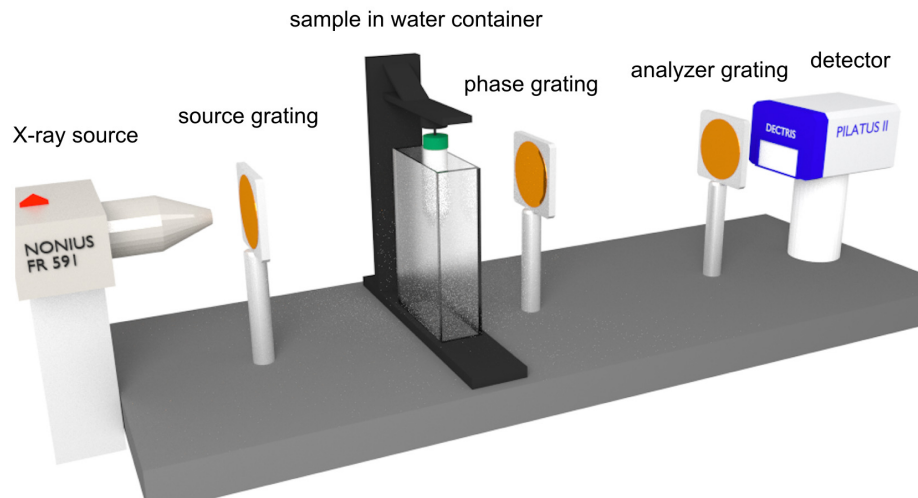
Figure 1. Schematic laboratory GBPC-CT setup. The setup consists of the X-ray source, three X-ray gratings, namely the source grating, the phase grating, and the analyzer grating, followed by the Pilatus II detector. The sample, which is immersed in a water container, is put directly in front of the phase grating. This figure is licensed under the Creative Commons Attribution (CC BY) and first published in Willner et al. [29].

the raw data [30] and used polynomial ramp correction of the phase-contrast projections [31]. The average interferometric visibility determined in an area of 420×190 pixels was 31.3, 30.9, and 11.6 % for 35 kVp, 40 kVp, and 50 kVp, respectively.

In our tomographic reconstruction of the 800 projections, we applied filtered backprojection using a Ram-Lak filter for the attenuation and a Hilbert filter for the phase-contrast data [32, 33].

For determining of the effective energy, we compared the experimental values of a known material – for example the PMMA rod in our case – with the theoretical energy dependent data. As we measured our object in a water container, the resulting data was the relative difference of the refractive index between the object and water. The comparison of this experimentally determined difference in the refractive index decrement to the theoretical differences – which are energy dependent – allowed to determine the effective energy. The calibration was performed for both the refractive index decrement δ and the attenuation coefficient μ.

Beam hardening correction was performed using an empirical polynomial approach similar to the one shown in [34]. The model function p was

$$p = p_0 + a p_0^3, \tag{1}$$

with the initial projection line integrals p_0 and the parameter a being determined in a homogeneous section through the sample until the effect of cupping artifacts are minimized. The parameter a was found to be $a = -0.32$. The new line integrals p were then used for the reconstruction.

2.2. Quantitative X-ray phase-contrast imaging

The quantity of interest in phase-contrast imaging is the complex index of refraction

$$n = 1 - \delta + i\beta, \tag{2}$$

where δ is the refractive index decrement and β is the imaginary part of the refractive index. The refractive index decrement can be related to the electron density ρ_e in absence of absorption

edges as

$$\delta = \frac{2\pi r_0 \hbar^2 c^2}{E^2} \rho_e, \tag{3}$$

where r_0 is the classical electron radius, $\hbar$ is the reduced Planck constant, c is the speed of light, and E is the energy [35].

The imaginary part of the refractive index β is related to the energy and material dependent absorption coefficient μ as

$$\beta = \frac{\mu}{2k}, \tag{4}$$

with k being the wave vector. As the sample is put in a water container, one measures the relative attenuation coefficient μ_{rel}. To access the absolute attenuation coefficient μ_{abs}, the absolute energy dependent attenuation coefficient of water has to be added to the relative attenuation coefficient

$$\mu_{abs} = \mu_{rel} + \mu_{H_2O}(E_{eff,\mu}), \tag{5}$$

with $E_{eff,\mu}$ being the effective energy of the attenuation signal. As described in the previous section (see Sec. 2.1), the latter can be determined using effective energy calibration with a known material like the PMMA rods here.

In grating interferometry, one determines the lateral phase-shift of the interference pattern ϕ, which is related to the phase-shift Φ of the wavefront and thus the complex index of refraction n by

$$\frac{1}{k}\frac{\partial \Phi}{\partial x} = \frac{p_2}{2\pi d}\phi, \tag{6}$$

with p_2 being the period of the analyzer grating and d the distance between the phase and the analyzer grating. The phase shift Φ is directly related to the refractive index decrement δ_{rel}, which signifies the refractive index decrement measured relative to water, as

$$\Phi = k \int \delta_{rel} dz, \tag{7}$$

in beam direction z. We calculate the effective energy of the refractive index decrement $E_{eff,\delta}$ using the PMMA rod in the same way like in the case of the attenuation coefficient. The absolute refractive index decrement δ_{abs} can be determined with the corresponding refractive index decrement of water δ_{H_2O} as

$$\delta_{abs} = \delta_{rel} + \delta_{H_2O}(E_{eff,\delta}). \tag{8}$$

This allows to determine experimentally the electron density

$$\rho_e = \frac{E_{eff,\delta}^2}{2\pi r_0 \hbar^2 c^2}\delta_{abs}. \tag{9}$$

The electron density can be theoretically calculated if the mass density ρ and composition of the material is known [26]:

$$\rho_e = \rho N_A \frac{\sum w_i Z_i}{\sum w_i A_i}, \tag{10}$$

where the weights w_i account for the fraction of atom i. Z_i is the atomic number, A_i the atomic mass number, and N_A Avogadro's number. The electron density of a single atom can be calculated by

$$\rho_e = \rho N_A \frac{Z}{A}. \tag{11}$$

2.3. Determination of the effective atomic number Z_{eff}

With the electron density and attenuation coefficient at hand, one can determine the effective atomic number Z_{eff}. In contrast to the electron density, the total attenuation coefficient still depends on both the energy and the atomic number. Assuming a single atom, the total attenuation coefficient is formed by

$$\mu = \rho \frac{N_A}{A} \sigma_{\text{tot}}(E, Z), \tag{12}$$

with σ_{tot} being the total atomic interaction cross section, which is related to the total electronic interaction cross section $\sigma_{\text{tot,e}}(E, Z)$ via $\sigma_{\text{tot}}(E, Z) = \sigma_{\text{tot,e}}(E, Z) \cdot Z$. The total atomic interaction cross section is based on three effects, namely the photoelectric (ph) effect as well as coherent (coh) and incoherent (incoh) scattering expressed as

$$\sigma_{\text{tot}}(E, Z) = \sigma_{\text{ph}}(E, Z) + \sigma_{\text{coh}}(E, Z) + \sigma_{\text{incoh}}(E, Z). \tag{13}$$

If we expand Eq. (12) with the atomic number and use Eq. (11), we get an expression which depends on the electron density, the atomic number, and the total absorption cross section

$$\mu = \rho_e \frac{\sigma_{\text{tot}}(E, Z)}{Z}. \tag{14}$$

Rearranging this expression leads to the central equation of this work to determine the effective atomic number Z_{eff}

$$\frac{\rho_e}{\mu} = \frac{Z_{\text{eff}}}{\sigma_{\text{tot}}(E, Z)}, \tag{15}$$

with the left side being the ratio of the electron density over the attenuation coefficient, which can be experimentally determined. $\sigma_{\text{tot}}(E, Z)$ can be accessed from tabulated data [36–38]. Equation (15) is equivalent to the resulting formula presented in Willner et. al [21]. Now we can calculate this ratio with GBPC-CT if we compare the experimental ratio for compound materials with the interpolated curve of the tabulated data using the effective energy E_{eff}. This leads then to the effective atomic number Z_{eff}.

Independent calculation of the atomic number to provide a theoretical reference is not trivial [39]. In this work, we use two references of the effective atomic number. As the first reference for the effective atomic number calculation, we used the following empirical formula

$$Z_{\text{eff}} = \sqrt[2.94]{\sum_i (w_i Z_i)^{2.94}}, \tag{16}$$

with w_i being the total fraction of electrons and Z_i being the atomic number of each component of the molecule [27, 40]. Different theoretical reference values for the effective atomic number are given by the XMuDat software, which is used as the second reference [41]. Replacing the factor 2.94 in Eq. (16) with 3.50 leads to the values presented in [41].

3. Results and discussion

3.1. Electron density and absorption coefficients

For determination of the electron density and the attenuation coefficients, we performed a tomographic scan of a phantom consisting of five different polymers at two tube voltages: 35 kVp and 50 kVp. Figure 2 illustrates the corresponding axial slices of the retrieved data. The phantom consists of low-density polyethylene (LDPE), polyoxymethylene (POM), polyetheretherketone (PEEK), Nylon, and polymethylmethacrylate (PMMA), embedded in a water container. Between Figs. 2(a) and 2(c), one observes difference in contrast in the attenuation signal, which originates

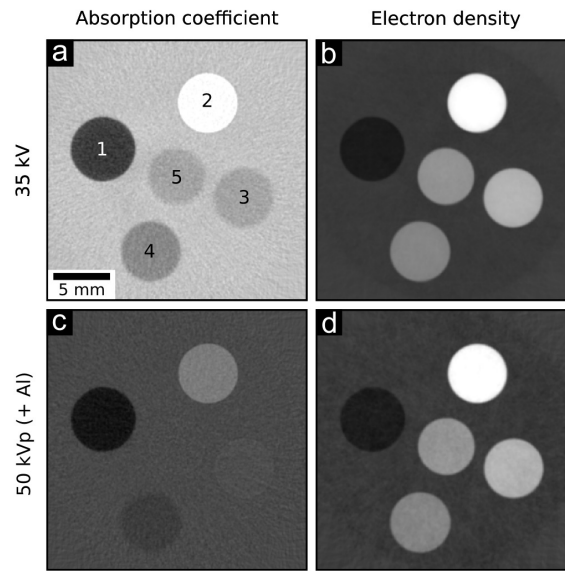Absorption coefficient   Electron density

Figure 2. Results of the phantom measurement at different source spectra. Axial slices of two scans at 35 kVp and at 50 kVp. The phantom consists of five different materials (1: LDPE, 2: POM, 3: PEEK, 4: Nylon, and 5: PMMA) embedded in a water surrounding. The absorption coefficients are displayed on the left and the electron density on the right. The quantitative GBPC-CT values can be found in Table 1 and the mass densities and chemical compositions of the materials can be found in Table 2. The attenuation coefficient μ is displayed linearly in an interval of $[0.2, 0.6]$ in 1/cm and the electron density ρ_e in an interval of $[300, 450]$ in e/nm^3. The experimental values presented here and in the other tables were determined as the mean of a certain volume and the respective error as the total standard deviation of the same data.

from the energy dependence of the attenuation coefficient. In the attenuation image (see Fig. 2(c)), the contrast between Nylon, PMMA, and the surrounding water is low. The electron density remains however at the same contrast level (see Figs. 2 (b) and 2(d)). Nylon and PMMA have similar electron density, but both materials can be differentiated in the attenuation signal in Fig. 2(a).

The experimental attenuation coefficients are plotted versus the electron densities in Figs. 3(a)

Table 1. Electron density values and linear attenuation coefficients of different polymers and water. The data was evaluated from phantom measurements at tube voltages of 35 kVp and 50 kVp (see Fig. 2). The theoretical reference values can be found in [37, 38]. The mass densities and chemical compositions of the materials can be found in Table 2.

| material	ρ_e (35 kVp) [e/nm^3]	ρ_e (50 kVp) [e/nm^3]	$\rho_{e,\text{theo.}}$ [e/nm^3]	μ (35 kVp) [1/cm]	$\mu_{\text{theo.}}$ (25.0 keV) [1/cm]	μ (50 kVp) [1/cm]	$\mu_{\text{theo.}}$ (34.5 keV) [1/cm]
LDPE	315.5 ± 0.8	316.2 ± 1.9	315.9	0.296 ± 0.010	0.299	0.231 ± 0.006	0.229
Nylon	377.2 ± 0.8	377.1 ± 1.9	376.0	0.418 ± 0.010	0.410	0.295 ± 0.006	0.291
PEEK	405.9 ± 0.9	405.3 ± 1.9	407.3	0.461 ± 0.009	0.457	0.321 ± 0.006	0.322
POM	451.5 ± 1.1	452.7 ± 2.1	452.3	0.607 ± 0.009	0.603	0.392 ± 0.006	0.390
PMMA	385.8 ± 0.9	385.9 ± 2.1	386.4	0.460 ± 0.010	0.459	0.315 ± 0.007	0.314
Water	333.4 ± 0.8	333.5 ± 2.0	334.2	0.509 ± 0.009	0.508	0.314 ± 0.006	0.313
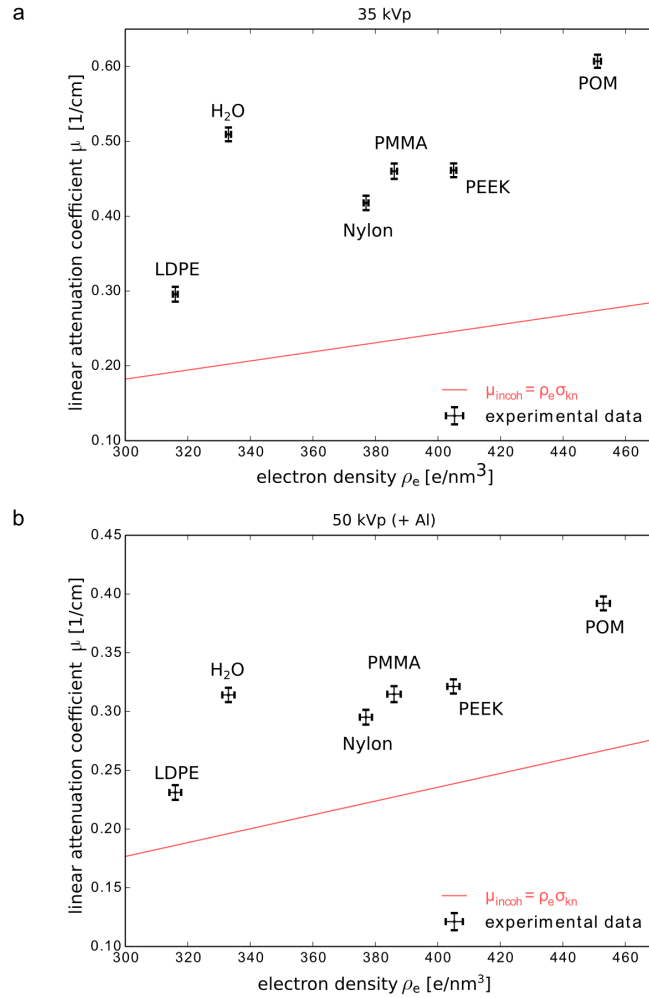
Figure 3. Scatter plots of the total linear attenuation coefficients versus the electron density of the two different setup voltages shown in Table 1. The experimental linear attenuation coefficients μ are plotted against the corresponding electron densities ρ_e obtained from GBPC-CT measurements at 35 kVp (a) and 50 kVp (b). Standard deviations are indicated by error bars and the red solid line represents the linear attenuation coefficient for Compton scattering μ_{incoh}.

and 3(b) for both energies of the setup to visualize the complementarity of both signals. The distance of the attenuation values to the Compton cross section decreases with increasing energy. Comparing PMMA and PEEK, one can see that the attenuation values are quite similar, especially at 50 kVp. Compared to Willner et al. [21], one can observe that the incoherent scattering part is not the dominating contribution to the total interaction cross section.

A quantitative comparison of the obtained data with theoretical values is summarized in Table 1. The mean and standard deviation of 150×30×30 voxels are compared for all materials with the corresponding theoretical values [37, 38]. The electron density is calculated according to Eq. (10). The effective energies of both scans were determined to $E_{eff,\mu} = 25.0\pm0.1$ keV for 35 kVp and $E_{eff,\mu} = 34.5\pm0.1$ keV for 50 kVp in the attenuation signal. The effective energy determined in the phase-contrast signal was $E_{eff,\delta} = 25.7\pm0.1$ keV for 35 kVp and $E_{eff,\delta} = 30.0\pm0.1$ keV for 50 kVp,
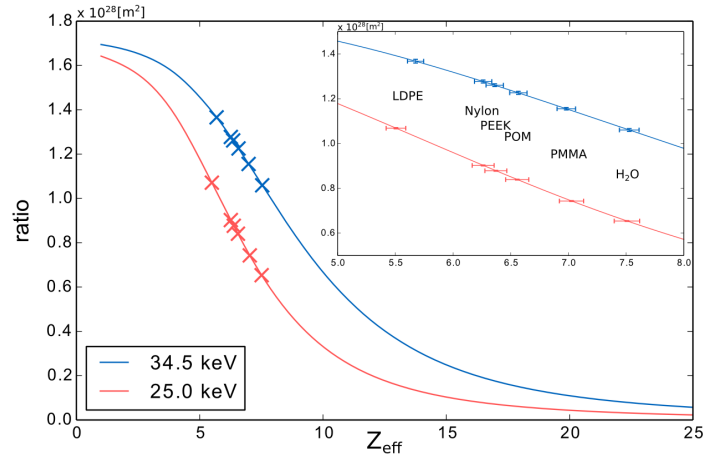
Figure 4. Determination of the effective atomic number for two different energies. The ratio represents both sides of Eq. (15). The right side of Eq. (15) is the theoretical ratio of the atomic number over the total cross section Z/σ_{tot} and shown by the continuous lines, which are based on the spline interpolated tabulated data. The left side of Eq. (15) is the ratio of the experimentally determined electron density over the linear attenuation coefficient ρ_e/μ of single elements, which is marked by the crosses ('x') and uses the experimental results from the phantom measurements shown in Fig. 2.

which were used for the calculation of the electron density and the effective atomic number in the following section. The differences between the effective energy of the attenuation contrast $E_{eff,\mu}$ and the effective energy of the phase-contrast $E_{eff,\delta}$ (see Table 1) originate in the different dependencies of the signals, since the DPC signal depends not only on the spectrum, but also on the visibility of the setup. The latter is formed by the spectrum, the setup design including the geometry, and the X-ray gratings. However, the effective energies for both modalities are quite similar, which can be explained by the way of determination of the effective energy. The position and the material type are essential for the effective energy determination, which is here the PMMA rod in the center of the tube. The composition of the polymers and their mass densities are presented in Table 2. All theoretical electron density values with exception of PEEK lie within the error margins of their respective standard deviations. The electron density values of PEEK are only slightly off, but still lie below 1 %. Since the other electron density values are in good agreement with the references, we assume that impurities could cause this slight deviation. The attenuation coefficients show also overall good agreement to literature values and other phase-contrast experiments [42, 43]. The average electron density resolution is approximately $1.0\,e/nm^3$ for the 35 kVp experiment and approximately $2.0\,e/nm^3$ for the 50 kVp measurement. Higher exposure times per phase step and thus higher total exposure time per DPC projection would increase the electron density resolution aside from a redesign of the setup [28].

3.2. Effective atomic number

With the experimental determination of the absorption coefficient and the electron density, we are now able to extract the effective atomic number Z_{eff} as described by Eq. (15). The calculated theoretical values are compared and plotted against the experimental results in Fig. 4. The interpolated curves determine the theoretical values for both calibrated effective energies. The experimentally determined ratio of ρ_e/μ is then compared with the interpolated reference data, thereby getting the effective atomic number corresponding to this ratio. The results are

summarized in Table 2. Compared to both provided references, the theoretical values with exception of LDPE lie within the error margins of the respective experimental effective atomic numbers Z_{eff}. The uncertainty of the calculation of the effective atomic number is based on Gaussian error propagation of the standard deviation of the attenuation coefficients, the electron density resolution, and the uncertainty of the calibration of the effective energy of 0.1 keV.

In comparison to Ref. 1 [27], the effective atomic numbers deviate slightly. The underlying formula (see Eq. (16)) is however an empirical approximation and not a ground truth [39]. The same statement can be made for Ref. 2 [41], which is based on the same formula like Ref. 1 and of the same empirical nature. However, those values were closer to our determined effective atomic number values of the phantom.

3.3. Effect of beam hardening

In a further GBPC-CT experiment, we assessed the impact of beam hardening on the electron density and effective atomic number. In order to simulate sufficiently strong beam hardening effects, we chose three different surrounding liquids, namely water, oil, and a 5% sodium chloride (NaCl) solution. A GBPC-CT experiment using air instead of a liquid was not feasible due to too strong phase-wrapping and beam hardening effects. The measurements were performed at constant voltage of 40 kVp, for which the GBPC-CT setup is optimized with respect to performance and thus visibility. The NaCl solution mimics tissue environment with high density like fibrous tissue and the oil is used to represent adipose tissue [44]. The phantom itself consists of four Eppendorf tubes filled with water, blood, a 5% sodium chloride (NaCl) solution, and oil, as the GBPC-CT setup is intended for biomedical research. For calibration, three PMMA rods were added.

Three different axial slices of the electron density ρ_{e} (see Figs. 5(a)-5(c)) and the corresponding slices of the effective atomic number Z_{eff} (see Figs. 5(d)-5(f)) were determined as described in the previous section (see Sec. 3.2). The PMMA rods (1) were used to determine an effective energy in all three data sets. The determined effective energies and electron density results are summarized in Table 3 and the effective atomic numbers Z_{eff} in Table 4.

The effective energy determined in the attenuation signal increases from oil (27.1 keV) over water (27.2 keV) to the NaCl solution (27.6 keV), the same is valid for the phase-contrast data (see Table 3). As already mentioned, the difference in effective energy between the two signals attenuation and electron density originates in the different dependencies of the two modalities. In a similar way compared to the experiment with different source spectra (see Sec. 3.1), the way of determination of the image signals reduces the differences in the effective energies between the different surrounding liquids.

Table 2. Comparison of the determined effective atomic number $\mathbf{Z}_{\text{eff}}$ with reference values. The theoretical effective atomic numbers of Ref. 1 were calculated from the elemental compositions of the materials according to Eq. (16). Ref. 2 uses a factor of 3.50 in Eq. (16) [41], the mass density ρ is based on the data provided by the manufacturer [45]. Nylon is of type 6,6.

material	chemical formula	ρ [g/cm^3]	Z_{eff} (ref. 1)	Z_{eff} (ref. 2)	Z_{eff} (25.0 keV)	Z_{eff} (34.5 keV)
LDPE	$[C_2H_4]_n$	0.92	5.44	5.53	5.49 ± 0.10	5.68 ± 0.08
Nylon	$[C_{12}H_{22}N_2O_2]_n$	1.14	6.12	6.21	6.26 ± 0.10	6.26 ± 0.08
PEEK	$[C_{19}H_{12}O_3]_n$	1.30	6.38	6.32	6.38 ± 0.10	6.36 ± 0.08
POM	$[CH_2O]_n$	1.41	6.95	7.03	7.03 ± 0.10	6.98 ± 0.08
PMMA	$[C_5H_8O_2]_n$	1.19	6.47	6.56	6.55 ± 0.10	6.57 ± 0.08
Water	H_2O	1.00	7.42	7.51	7.51 ± 0.10	7.54 ± 0.08

Table 3. Relative comparison of the electron density of the liquids phantom in dependence of different surrounding liquids at 40 kVp. Results of three phantom measurements with different surrounding liquids are shown. With exception of PMMA and water, no theoretical reference values are given (see Table 1).

surrounding liquid		water	oil	5 % NaCl
$E_{\text{eff},\mu}$	[keV]	27.2 ± 0.1	27.1 ± 0.1	27.6 ± 0.1
$E_{\text{eff},\delta}$	[keV]	27.0 ± 0.1	26.9 ± 0.1	27.3 ± 0.1
1 - PMMA	[ρ_{e} in e/nm^3]	386.2 ± 1.0	386.4 ± 1.0	385.9 ± 1.6
2 - blood	[ρ_{e} in e/nm^3]	354.0 ± 1.0	355.1 ± 0.9	353.7 ± 1.1
3 - water	[ρ_{e} in e/nm^3]	333.9 ± 1.0	333.8 ± 0.9	334.2 ± 1.0
4 - 5% NaCl	[ρ_{e} in e/nm^3]	343.0 ± 1.0	344.3 ± 0.8	342.4 ± 1.5
5 - oil	[ρ_{e} in e/nm^3]	305.9 ± 0.9	305.1 ± 1.0	307.4 ± 1.0

Table 4. Relative comparison of the effective atomic number of the liquids phantom in dependence of different surrounding liquids at 40 kVp. Results of three phantom measurements with different surrounding liquids are shown. With exception of PMMA and water, no theoretical reference values are given (see Table 2).

surrounding liquid		water	oil	5 % NaCl
1 - PMMA	[Z_{eff}]	6.58 ± 0.07	6.55 ± 0.06	6.58 ± 0.08
2 - blood	[Z_{eff}]	7.61 ± 0.06	7.61 ± 0.06	7.58 ± 0.07
3 - water	[Z_{eff}]	7.49 ± 0.08	7.50 ± 0.06	7.47 ± 0.07
4 - 5% NaCl	[Z_{eff}]	8.37 ± 0.07	8.38 ± 0.06	8.30 ± 0.07
5 - oil	[Z_{eff}]	5.92 ± 0.09	5.97 ± 0.08	5.98 ± 0.09

Comparing the electron density results in Table 3, the absolute values for water and PMMA are in good agreement with reference values (see Table 1). The relative differences of the other liquids are within the range of the noise except for the blood sample and the NaCl solution in the oil surrounding liquid and the oil in the NaCl solution surrounding liquid. Though, the maximum deviation of the electron density is still below 1 %. The electron density resolution determined in the PMMA rods is ranging from 1.0 to 1.6 e/nm^3.

Regarding the effective atomic number (see Table 4), the absolute effective atomic numbers for PMMA and water are in good agreement with the results shown in Table 2. Comparing the different surrounding liquids, almost all effective atomic numbers lie within the margin of the standard deviation except for oil in the NaCl solution. However, beam hardening correction was necessary for oil being the surrounding liquid to provide sufficient quality of the data. Here, we used polynomial beam hardening correction similar to the one shown in [34] and presented in Sec. 2.1. The quantitative differences in the effective atomic number Z_{eff} with and without beam hardening correction lie below 5%, which was the case for oil in the oil surrounding liquid. Without this correction the results would deviate strongly as strong beam hardening of the spectrum causes streaks and cupping artifacts leading to reduced quality of the quantitative data. In contrast, the water and NaCl solution act as sufficiently well filtering surrounding liquids without the need for additional beam hardening correction.

4. Conclusion

In this work, we illustrate how to determine the effective atomic number with a polychromatic, laboratory GBPC-CT setup in a single tomographic scan based on the method shown in Willner et al. [21], where a monochromatic synchrotron beam of 82 keV was used. The results of the effective atomic numbers and the electron density values turned out to be quantitatively reliable
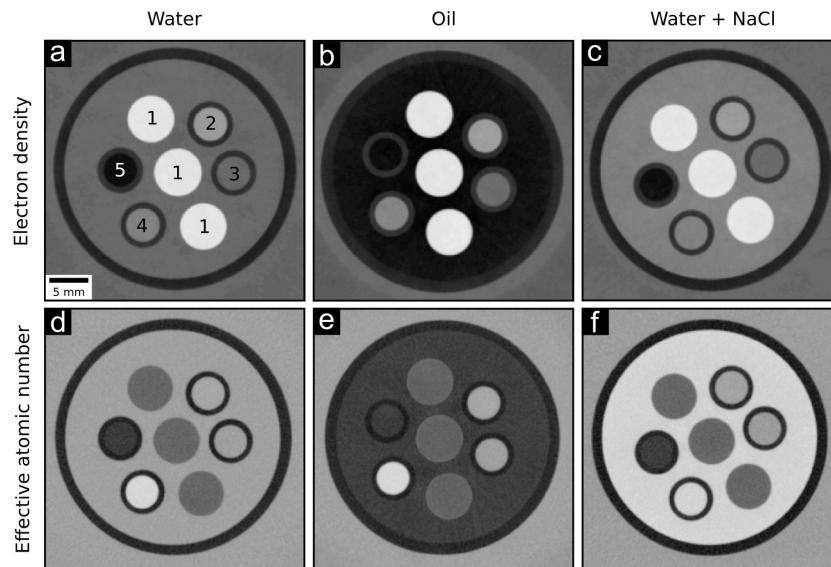
Figure 5. Phantom experiments with different surrounding liquids. Quantitative GBPC-CT results of phantom measurements with different surrounding liquids visualize the effect of the polychromatic X-ray spectrum on the measured values of the electron density and the effective atomic number due to beam hardening. The top row shows the electron density ρ_e, the bottom row the effective atomic number Z_{eff}. Subfigures (a) and (d) show an axial slice of the phantom immersed in water, subfigures (b) and (e) show the same phantom measured in oil, and subfigures (c) and (f) represent the experiment in the 5% NaCl solution as surrounding liquid. The components and results of the phantom are listed in Tables 3 and 4. The electron density ρ_e is linearly displayed in an interval of $[300, 400]$ in e/nm^3 and the effective atomic number Z_{eff} in an interval of $[5, 9]$. The tube voltage was $40\,kVp$.

in the investigated energy range. If surrounding liquids do not act as sufficiently strong filters of the spectrum as it was in the case of oil, beam hardening correction is necessary to obtain reliable quantitative effective atomic numbers. The measured electron density varied only marginally for different surrounding liquids and was not as prone to beam hardening as the attenuation coefficient [46].

In comparison to related work, the approach used here needs only one calibration for the effective energy. Qi et al. used multiple material calibration neglecting the coherent part of the cross section σ_{coh}. There, the exponential fit depends strongly on the quality of the reference effective atomic numbers, which can limit the precision of the method [24, 27]. DECT also provides the effective atomic number as well as the electron density and is already clinically established in contrast to the experimental stage of GBPC-CT. Additionally, the polychromatic laboratory GBPC-CT experiments presented here to determine the effective atomic number were only performed for X-ray tube voltages up to $50\,kVp$, which is no limit for DECT. However, DECT needs complex calibration, whereas GBPC-CT employs only one simple calibration to access the electron density and the effective atomic number.

Measuring at lower energies in comparison to the $82\,keV$ presented in Willner et al. [21] is beneficial for biomedical GBPC-CT application, due to better interaction contrast in the energy range used here. In addition to Willner et al. [21], we show that the approach also works if the incoherent scattering part is not the dominating contribution in the total interaction cross section (see Fig. 3). The validity of the results in this work is shown only for samples with relatively low effective atomic numbers ($Z_{eff} \leq 8$). At this GBPC-CT setup with a maximum tube voltage

of 50 kVp, experiments of materials with higher atomic number are of limited quality due to increased noise and expected beam hardening artifacts. In order to investigate the electron density and the effective atomic number of samples with higher atomic numbers or thicker samples, respectively, a new GBPC-CT setup for at higher polychromatic energies would have to be designed. Additionally, the use of spectral detector technique could allow one to increase the performance of the method by reducing beam hardening artifacts and avoid the effective energy calibration.